Atomization of a High Speed Jet

Zhiliang Xu[§‖], Myoungnyoun Kim[§‖], Wonho Oh[‡‖,**], James Glimm[‡§‖,**], Roman Samulyak[§], Xiaolin Li[‡**] and Constantine Tzanos[¶]

April 14, 2005

Abstract

A numerical study of atomization, *i.e.* breakup of a high speed jet and spray formation, is presented using the Front Tracking method in 2D. The high speed flow in the nozzle gives rise to cavitation, *i.e.* a mixed liquid-vapor region. To represent the state of the mixed phase, two different equation of state (EOS) models, a homogenized model and a discrete vapor bubble model, were used. In the homogenized model, the vapor-liquid mixture is treated as a single pseudofluid. In the discrete vapor bubble model, the mixed vapor-liquid mixture is modeled as a system of pure phase domains (vapor and liquid) separated by free interfaces. The major conclusion is that the jet breakup and spray characteristics depend strongly on the choice of EOS model, with only the discrete vapor bubble model producing breakup and plausible agreement with experimental data.

[‡]Department of Applied Mathematics and Statistics, University at Stony Brook, Stony Brook, NY 11794-3600.

[§]Computational Science Center, Brookhaven National Laboratory, Upton, NY 11793-5000.

[¶]Reactor Analysis and Engineering, Argonne National Laboratory, Argonne, IL 60493

[‖]This research is supported in part by the U.S. Department of Energy, TSTT at BNL with Contract No. DE-AC02-98CH10886, and TSTT at SB with Contract No. DEFC0201ER25461.

[**]Supported in part by the U.S. Department of Energy, Contract Numbers DEFG0290ER25084, and National Science Foundation Contract No. DMS0102480.

1 Introduction

In the high speed jet, the mechanisms of atomization, *i.e.* jet breakup and spray formation, are a challenge to modern hydrodynamics. To predict jet breakup, various theories [1] and engineering models such as the Taylor analogy breakup (TAB) [2], enhanced TAB [3] and the Dynamic Drop Breakup model [4] have been proposed. These spray models are used in engine simulations. They have successfully calculated macroscopic post breakup features such as spray penetration and spray angle. But they do not reproduce the detailed features of breakup such as the droplet sizes and velocities. In this paper, we conduct a first principles simulation study of jet atomization, using the 2D axisymmetric front tracking code *FronTier* [5, 6, 7, 8]. The main conclusion is that modeling of the mixed phase region in terms of finite sized vapor bubbles in the liquid is a critical aspect of the jet atomization. We believe this to be the first numerical study of the atomization process at this level of detail in the modeling of the related physics.

In the simulations, fluid and jet nozzle parameters have been chosen that are typical of diesel jet fluid injection, following experiments performed at ANL [9], see Fig. 1. The nozzle diameter is 0.178 mm and its length is 1 mm. A finite pulse of diesel fuel is injected into a chamber of SF_6 (a heavy, inert gas chosen to emulate the density of compressed air in a diesel engine). In 0.3 msec, the pressure of injected fuel rises linearly from 1 bar to 500 bar, then it is maintained at this level for 0.4 msec, and subsequently, it drops linearly to 1 bar over 0.1 msec. Synchrotron x-ray imaging of fuel flow parameters such as mass distribution of fuel and the jet tip velocity evolution [9, 10, 11, 12] provide important information for the validation of numerical experiments.

Jet breakup is divided into four regimes [13, 14] due to different dominant forces acting on the jet, namely, the Rayleigh breakup regime, the first wind-induced regime,

the second wind-induced regime, and the atomization regime. The onset of atomization is predicted by Reitz in [14] to occur when

$$\frac{\rho_1}{\rho_2} > K f(T)^{-2} \ , \tag{1}$$

where subscripts 1 and 2 refer to liquid and ambient gas respectively, a convention followed in the rest of the paper. The parameter K is a function of the nozzle geometry given by the empirical equation

$$K = (0.53\sqrt{3.0 + (l/2a)} - 1.15)/744 \tag{2}$$

which accounts for the internal nozzle flow effects. Here l is the nozzle length and $2a$ is its diameter. Taylor's parameter T is given by

$$T = \frac{\rho_1}{\rho_2}(\mathrm{Re}_1/\mathrm{We}_1)^2 \ , \tag{3}$$

where Re is the Reynolds number and We is the Weber number. The function $f(T)$ is approximated as $f(T) = \frac{\sqrt{3}}{6}(1 - \exp(-10T))$. For the diesel jet studied in this paper, the jet tip velocity ranges from 70 m/sec to 100 m/sec. With liquid surface tension $\sigma = 1.96 \times 10^{-2}$ kg/sec^2, density $\rho_1 = 0.66$ g/cm^3, viscosity $\mu = 0.4$ cP and ambient stagnant gas density $\rho_2 = 0.00597$ g/cm^3, Eq. (1) becomes $\frac{\rho_1}{\rho_2} \cong 111 > 0.007$ which indicates that the breakup is in the atomization regime.

We consider the breakup regimes in more detail. Kelvin-Helmholtz (KH) instability will be suppressed [15] if

$$(U_1 - U_2)^2 < \frac{2}{\alpha_1 \alpha_2}\sqrt{\frac{\sigma \mathrm{g}(\alpha_1 - \alpha_2)}{\rho_1 + \rho_2}} \tag{4}$$

where U_1 is the liquid velocity, U_2 is the gas velocity, g $= 981$ cm/sec^2 is the gravity, $\alpha_1 = \frac{\rho_1}{\rho_1+\rho_2}$ and $\alpha_2 = \frac{\rho_2}{\rho_1+\rho_2}$. For this diesel jet, we have

$$\frac{2}{\alpha_1 \alpha_2}\sqrt{\frac{\sigma \mathrm{g}(\alpha_1 - \alpha_2)}{\rho_1 + \rho_2}} \cong 37927 \text{ cm}^2/\text{sec}^2 \ , \tag{5}$$

which is less than the typical velocity difference between liquid jet and gas $(U_1 - U_2)^2 \cong 10^8$ cm^2/sec^2. Thus the jet surface is KH unstable. The most unstable surface mode has a wavenumber

$$k_0 = \sqrt{\frac{\mathrm{g}(\rho_1 - \rho_2)}{\sigma}} \cong 5.7 \text{ /cm} . \tag{6}$$

The corresponding wave length of this mode is about 1.1 cm.

The breakup of a low-speed jet in the Rayleigh breakup regime or first wind-induced regime is caused by the growth of long-wavelength, small amplitude disturbances on the jet surface. As the jet velocity increases, the maximum growth rate w_m of an initial perturbation on the jet surface occurs at wavenumbers k [13] larger than those of the first wind driven regime. Jet breakup in the wind-induced regime is thought to be due to the unstable growth of short wavelength surface waves. In the second wind-induced breakup regime, $ka > 1$, while in the atomization regime, $ka \gg 1$. For the parameters of the diesel jet studied here, nozzle radius is $a = 0.089$ mm, and $k_0 a$ is about 0.05. This shows that the KH instability governed by long wavelength waves as shown in Eq. (6) can not be the primary driving force for the breakup of this atomized jet.

For a high-speed jet, the mechanism of the breakup remains a research issue. Many parameters such as the nozzle shape, the velocity and the internal nozzle flow pattern, such as the turbulence of the jet, cavitation and the thermodynamic states of liquid and gas could be possible mechanisms responsible for jet breakup and atomization. Among these flow patterns, cavitation has been centered as a key phenomenon connecting nozzle flow to spray formation. Bergwerk [16] implied that liquid cavitation inside the nozzle could create pressure disturbances in the flow leading to atomization. Chaves *et al.* [17] have captured cavitation in a 0.2 mm nozzle photographically. Arcoumanis *et al.* [18] photographed cavitating flow in a 20-times scaled injector tip. Also in [19], simulations have been presented for cavitation of 2D

asymmetric nozzles. The droplet diameter and its distribution have also been studied experimentally in [20]. For the nozzles used in these experiments, it was shown that the droplet distribution is largely between 3 and 4 microns with a number frequency up to 38%. Large droplets up to a diameter of 14 microns were also observed.

Our goal is to model the spray at a micro-physical level, where individual droplets are created. Simulations were performed for flow in a diesel injector nozzle using a 2D axis-symmetric geometry. The large density difference between the liquid and vapor and the complex free surfaces which separate two fluids make the numerical simulation difficult. To overcome these difficulties, we used *FronTier*, a front tracking [5, 6, 7, 8] hydro multiphysics code to track these complex surfaces in combination with Berger-Colella [21] adaptive mesh refinement (AMR).

To describe cavitation, which involves liquid-vapor two-phase flow, two equation of state (EOS) models for the mixed phase region are used, *i.e.* a homogenized model and a discrete vapor bubble model with vapor bubbles of finite size. The homogenized model describes multiphase flows by averaged equations. In the discrete vapor bubble model, the liquid-vapor mixture is modeled as pure phase domains (vapor bubble and liquid diesel fuel) separated by free interfaces. The predicted results produced by these two models are compared.

The paper is organized as follows. In Section 2, the numerical algorithms used for the simulation are described. In Section 3, the internal nozzle flow is studied. In Section 4, a homogenized EOS model is used to simulate the jet flow, and the result is discussed. In section 5, a discrete vapor bubble model is formulated. To allow the creation of vapor bubbles, a dynamic bubble insertion algorithm is developed and a new type of Riemann problem associated with liquid-vapor phase change is solved. Section 6 contains simulation results using the discrete vapor bubble model. Section 7 discusses the differences in the predicted results of two models, and the conclusions

are drawn there.

2 Numerical Algorithms

To model the high pressure pulse imposed on the fuel inlet, a time dependent pressure boundary condition was introduced. For subsonic isentropic flow, this prescribed pressure gives a complete inlet boundary condition. A flow-through boundary condition is used at the flow outlet and a no slip condition is used at the nozzle wall.

The diesel liquid is treated as a viscous heat conducting fluid. Because the thermal conductivity and the viscosity are both small, the Navier-Stokes (NS) equations are solved with an explicit algorithm. In the interior, for the convection terms of the NS equations, a MUSCL scheme [22] is used, which is 2nd order accurate in both space and time, and for the diffusion terms, central differencing is employed. To update a front solution, an operator splitting method is used, which divides into a normal front propagation step and a tangential front propagation step. In the normal front propagation step, a front is propagated to a new position in its normal direction by solving a generalized Riemann problem. The method of characteristics is used to update the states on the two sides of the front at this new position. In the tangential front propagation step, a first order Lax-Friedrichs scheme is applied.

We adopted the Berger-Colella [21] adaptive mesh refinement (AMR) to the front tracking method by merging *FronTier* with the *Overture* code, the AMR package developed at Lawrence Livermore National Laboratory. All material interfaces are tracked. Cells where the estimated errors are larger than some threshold, and cells which contain, or are sufficiently close to the interface are refined. The refinement of the cells close to the interface is implemented by using a controlling parameter which specifies the minimum distance from the front to the fine grid boundary. Thus the tracked interfaces are all covered by the finest level patches. *FronTier* is fully paral-

lelized and the AMR package was parallelized in a manner compatible with *FronTier*. A global domain is divided into rectangular subdomains. Each subdomain is assigned to a single processor and adaptively refined there. The *Overture* error estimator does not communicate through subdomain boundaries. To minimize the influence of the subdomain decomposition on the refinement, ghost patches are created according to the refinement. For example, consider two adjacent subdomains, where one has a finer refinement (say level l) aligned to the common subdomain boundary, while the other does not. The subdomain without level l refinement also creates a level l patch aligned to the common subdomain boundary with specified depth (usually 4 to 6 cells) and length to match the refined level l patch of its neighboring subdomain.

To balance the workload on different processors, we need to distribute AMR patches from processors with excessive workload to processors with deficient workload. We refer to [23] for a detailed description of this work. For the simulations presented in this paper, 3 levels of refinement with a refinement factor 2 were used. The base level has 170×1000 cells on the 1.513 mm $\times$ 8.9 mm domain, which is half of the injection reservoir and combustion chamber as shown in Fig. 1. The finest grid level has a mesh resolution of 2 microns.

3 Flow in the Nozzle

In this section, we present the results of numerical simulations of the flow in the nozzle. We assume the flow is composed of pure liquid whose EOS is given by a stiffened polytropic equation

$$P + \gamma P_\infty = (\gamma - 1) * \rho * (E + E_\infty) \tag{7}$$

with adiabatic exponent $\gamma = 3.19$, stiffening constant $P_\infty = 3000.5$ g/cm $\cdot$ ms^2 and energy translation $E_\infty = 4851.6$ cm^2/ms^2. Here ρ is the density, P is the pressure

and E is the specific internal energy. Because of the symmetry, only 1/2 of the nozzle was simulated, which has a 0.088 mm $\times$ 1.0 mm domain. This domain is discretized into 80 $\times$ 910 cells.

With a liquid density 0.66 g/cm^3, mean velocity 100 m/sec, and dynamic viscosity 0.004 g/(cm.sec), the Reynolds number Re $= 3.3 \times 10^4$ greatly exceeds the critical value for transition to turbulence. Strong vorticity was observed only near the nozzle boundary layer, which was essentially laminar in nature (See Fig. 2). When the fluid enters a circular pipe from a container, the velocity distribution in the cross-section varies with the distance from the pipe entrance. The nearly uniform velocity distribution near the entrance gradually transforms into a parabolic profile, and if the flow Reynolds number is greater than the critical value, a transition takes place. The transition from laminar to turbulent flow is accompanied by noticeable changes. The flow goes through an initial instability, as unstable two dimensional Tollmien-Schlichting (T-S) waves propagate in the direction of the free stream. This is followed by three dimensional T-S waves, cascading vortex breakdown, formation and growth of turbulent spots and full turbulence. The distance from the pipe entrance to the location where the parabolic profile is first fully developed constitutes the theoretical initial length of the laminar flow and its magnitude is approximately

$$l = 0.03d \times \mathrm{Re}\ , \tag{8}$$

where d is the pipe diameter [24]. For Re $\cong 10^4$, it is about 300 pipe diameters. In turbulent flow, this length is much shorter. According to the measurements performed by H. Kirsten [25] and by J. Nikuradse [26], it ranges from 25 to 100 pipe diameters. Because the length of the nozzle simulated here is five pipe diameters, transition to fully turbulent flow is not expected.

The simulation showed regions with large values of "negative pressure" (Fig. 3), which indicates the formation of cavitation. Figure 3 shows snap shots of pressure

field at consequent times, from the top frame to the bottom one, t = 2.54×10^{-5} sec, 2.66×10^{-5} sec, and 2.92×10^{-5} sec. The negative pressure first appears at the upstream corner. Increasing inlet pressure causes the negative pressure to extend throughout the nozzle. To simulate the cavitation, two different EOS models were used. The differences in the simulation results demonstrate the importance of the discrete vapor bubble approach to cavitation, which is the main conclusion of this paper.

4 The Homogenized Model

4.1 Model Formulation

The homogenized EOS consists of three branches; pure vapor, pure liquid and a liquid-vapor mixture. The entire process is treated as isentropic, which reduces the number of independent thermodynamic variables to one. The density is chosen as this independent parameter, and the other thermodynamic parameters are functions of density. A gamma law gas EOS is used to model the vapor branch while a stiffened polytropic gas EOS (7) models the liquid branch. A homogeneous equilibrium model [27, 28] is used to connect the liquid and the vapor branches along an isentrope for the liquid-vapor mixture. The sound speed of the mixed phase [27] is

$$\frac{1}{c^2} = (\beta\rho_{\mathrm{sat,v}} + (1-\beta)\rho_{\mathrm{sat,l}}) \left(\frac{\beta}{\rho_{\mathrm{sat,v}} c^2_{\mathrm{sat,v}}} + \frac{1-\beta}{\rho_{\mathrm{sat,l}} c^2_{\mathrm{sat,l}}} \right) , \tag{9}$$

where $\rho_{\mathrm{sat,v}}$, $\rho_{\mathrm{sat,l}}$, $c_{\mathrm{sat,v}}$ and $c_{\mathrm{sat,l}}$ are the saturated vapor and liquid density and sound speed respectively, and β is the void fraction, that is

$$\beta = \frac{\rho - \rho_{\mathrm{sat,l}}}{\rho_{\mathrm{sat,v}} - \rho_{\mathrm{sat,l}}} . \tag{10}$$

The derivation of this EOS model and for the detailed parameters used to fit the experimental properties of the diesel fuel are presented in [29]. Figure 4 displays a plot of the pressure *vs.* specific volume.

4.2 A Mach Number Analysis

In the mixed phase region, the speed of the sound is small, for example, if the void fraction $\beta = 0.5$, it is about 15% of the speed of the sound in vapor. More specifically, the speed of the sound of the vapor is about 200 m/sec and the sound speed in the mixed phase region is 30 m/sec. The velocity of the flow in the jet ranges from 160 m/sec to 200 m/sec at the nozzle exit, and is about 100 m/sec at the leading edge. Thus, the mixed phase region is highly supersonic with Mach number $M > 5$.

The KH instabilities have been studied through the vortex sheet model. In the two dimensional case, it is known that subsonic compressible vortex sheets are unstable, while supersonic compressible vortex sheets are neutrally linearly stable. The growth rates of KH instabilities in compressible fluids decrease as the Mach number increases [30]. This result agrees formally with the theory for incompressible fluids as the sound speed goes to ∞. In an inviscid fluid, the effect of compressibility on the linear KH instability has been studied by linear theory in [31]. It is shown that the growth rate of the linear KH instability in the subsonic flow (which mimics the incompressible case) is greater by a factor of 2 than that in the supersonic flow. It turns out that a highly supersonic flow strongly suppresses KH instability formation. Because of the suppression, the small wavelength perturbations produced by KH instabilities which are resolved by the current grid resolution, are not amplified to produce significant breakup in the simulated jet, and little breakup is produced.

4.3 Numerical Results

This section presents simulations performed with the homogenized model. Fig. 5 shows a density plot of the jet. The simulation shows a slow growth of surface perturbations without any indication of breakup. The light spots in Fig. 5 represent a liquid-vapor mixture, *i.e.* cavitation. They are located at the center of an incipient KH vortex roll up perturbation at the jet surface. The size of the liquid-vapor mixture region does not grow significantly during the simulation. This is in disagreement with the results of a pure liquid jet shown in Section 3, which showed large regions of "negative pressure". A possible explanation of the failure of the homogenized EOS model to produce breakup is the suppression of breakup in the high Mach number flow.

5 The Discrete Vapor Bubble Model

5.1 Critical Bubble Radius

The discrete vapor model takes account of the finite size effects of the vapor bubbles in the mixed phase flow regime. To model the diesel liquid, the stiffened gamma law gas EOS of Section 3 is used. The mixed phase regime is modeled by vapor bubbles of finite size inserted into the diesel liquid, and the vapor is modeled by a gamma law gas EOS with $\gamma = 1.05$.

Vapor bubbles are formed by liquid vaporization when the liquid pressure P fluctuates and falls below the saturated vapor pressure P_v at constant temperature. The pressure fluctuation $P_v - P$, which is a positive quantity if $P_v > P$, is called tension $\triangle P$. Physically, a vapor bubble will appear whenever it is thermodynamically favorable. Cavitation is the result of rapid growth of vapor nuclei that become

unstable due to a change in ambient pressure. If the maximum size of a nucleus is defined by the radius R_C (critical radius), then at equilibrium, the magnitude of the tension $\triangle P_C$ the liquid is able to sustain is given by [32, 33]

$$\triangle P_C = \frac{2\sigma}{R_C} \ , \tag{11}$$

where σ is the surface tension of the liquid. So the critical radius of a cavitation bubble is

$$R_C = \frac{2\sigma}{\triangle P_C} \ . \tag{12}$$

To create such a nucleus with critical radius R_C, a critical energy $E_{CR} = \frac{16\pi\sigma^3}{3\triangle P_C^2}$ [32, 33] must be deposited into the liquid to break the barrier against nucleation. This critical energy E_{CR} accounts only for surface energy and the gain in volume energy. The energy needed to convert liquid to vapor (heat of vaporization) is neglected, because it is relatively small. One can write a nucleation rate J

$$J = J_0 \text{exp}^{E_{CR}/(k_b T)} \ , \tag{13}$$

per unit volume and per unit time. Here k_b is the Boltzmann's constant, T is the liquid temperature, and J_0 is a factor of proportionality defined as

$$J_0 = N \left(\frac{2\sigma}{\pi m} \right)^{1/2} \ , \tag{14}$$

where N is the number density of the liquid (molecules/m^3) and m is the mass of a molecule. Thus the nucleation probability Σ in a volume V during a time period t is [34]:

$$\Sigma = 1 - \text{exp}^{\left(-J_0 V t \text{exp}^{(-E_{CR}/(k_b T))}\right)} \ . \tag{15}$$

Equations (12) - (15) can be used to compute the negative pressure threshold P_C needed to create cavitation bubbles for a given radius and nucleation probability.

In this work, we use a nucleation probability $\Sigma = 0.5$, and the negative pressure threshold P_C is given by

$$P_C \cong -\left(\frac{16\pi\sigma^3}{3k_bT\ln(J_0Vt/\ln 2)}\right)^{1/2} . \tag{16}$$

In the simulations, computational grid spacing $\triangle x$, which is about 2 microns, allows creation of a cavitation bubble with a minimum radius of 4 microns ($2\triangle x$). For $t = 10^{-9}$ sec, which is a typical value for a numerical time step of the simulations presented here, and V the nozzle volume, Eq. (16) gives for P_C a value of the order of -10 bar.

5.2 Dynamic Creation of Vapor Bubbles

We use an inserted bubble radius of $r = 2\Delta x$, where Δx is the mesh size. If a bubble evolves to a radius less than $2\Delta x$, it is deleted by the numerical routines. We also define the bubble spacing h as the distance between the centers of two bubbles. For a nucleation probability $\Sigma = 0.5$ and bubble radius $2\triangle x$, we have $h = 8\Delta x$.

The dynamic bubble creation algorithm proceeds as follows. In each cell at every time step, it is checked whether the liquid pressure p is less than -10 bar. Here -10 bar is the negative pressure threshold P_C estimated in Section 5.1. If there is a 4×4 block of cells that all have $p < -10$ bar centered in a larger $(4\Delta x + 2r) \times (4\Delta x + 2r)$ region which does not contain bubbles, a circular bubble of radius $r = 2\Delta x$ is inserted in this block. To define the vapor bubble states, the average temperature $\overline{T}$ and velocity $\overline{U}$ of the liquid that occupied these 4×4 cells are used. From the static Clausius-Clapeyron relation, the initial vapor pressure is set to be $P = P_{\rm sat}(\overline{T})$, which is the saturated liquid-vapor pressure $P_{\rm sat}(T)$ at a temperature $\overline{T}$. The vapor density is computed from the EOS. The initial vapor bubble velocity is set to be $\overline{U}$.

The discrete vapor bubble model for the simulation of linear (sound) and nonlin-

ear (shock) waves in liquids containing small non-dissolvable gas bubbles has already been validated using experimental data [35]. In [35], the number of bubbles remained constant during the simulation, while in the simulation of cavitation, bubbles can be dynamically created and destroyed. An application of the discrete vapor bubble model for the description of cavitation in mercury has been presented in [36]. Simulations were performed at conditions typical for the Muon Collider target experiments. Juric and Tryggvason [37] also used the discrete vapor bubble model to simulate film boiling.

5.3 Dynamic Phase Boundaries for Compressible Fluids

The complete description of the phase change has to take into account the coupling of surface tension, latent heat, interphase mass transfer, discontinuous material properties and interface dynamics. Earlier efforts [38, 39] to simulate the phase change concentrated on simple models of vapor bubble dynamics. Numerical methods to model phase change in a fluid flow have only recently become available. Welch [40] used a 2D moving mesh finite volume method to simulate liquid-vapor flow with phase change. Juric and Tryggvason [37] proposed a front tracking method based on techniques for isothermal multiphase flows. In [37], the liquid is considered as incompressible, and interfacial terms for surface tension, mass transfer and latent heat are added as delta functions that are non-zero only at phase boundaries.

In the model presented here, viscosity and the surface tension on the interface are neglected. The phase transition is then governed by the compressible Euler equations with heat diffusion,

$$\rho_t + (\rho u)_x = 0 \tag{17}$$

$$(\rho u)_t + (\rho u^2)_x + p_x = 0 \tag{18}$$

$$(\rho E)_t + (\rho E u + p u - \kappa T_x)_x = 0 \ , \tag{19}$$

where subscripts t and x are used to denote derivatives with respect to time and space respectively, $E = 1/2(u^2) + \epsilon$ is the total specific energy, ϵ is the specific internal energy, p is the pressure, κ is the thermal conductivity and T is the absolute temperature.

If the phase boundary is treated as a sharp interface, integration of the governing equations across the interface yields the jump conditions for the dynamic phase boundary

$$[\rho u] = s[\rho] \tag{20}$$

$$[\rho u^2 + P] = s[\rho u] \tag{21}$$

$$[\rho u E + P u - \kappa T_x] = s[\rho E] \ , \tag{22}$$

where s is the speed of the moving phase boundary, and the symbol $[U] = U_{\text{left}} - U_{\text{right}}$ means a jump across the phase boundary. Eq. (20)-(22) give

$$\rho_{\text{v}}(u_{\text{v}} - s) = \rho_{\text{l}}(u_{\text{l}} - s) \tag{23}$$

$$\rho_{\text{v}}(u_{\text{v}} - s)^2 + p_{\text{v}} = \rho_{\text{l}}(u_{\text{l}} - s)^2 + p_{\text{l}} \tag{24}$$

$$(\rho_{\text{v}} E_{\text{v}} + p_{\text{v}})(u_{\text{v}} - s) - \kappa_{\text{v}} T_{\text{v},x} = (\rho_{\text{l}} E_{\text{l}} + p_{\text{l}})(u_{\text{l}} - s) - \kappa_{\text{l}} T_{\text{l},x} \ , \tag{25}$$

and the change of energy during the phase transition is

$$\epsilon_{\text{v}} + \frac{p_{\text{v}}}{\rho_{\text{v}}} = \epsilon_{\text{l}} + \frac{p_{\text{l}}}{\rho_{\text{l}}} + Q_{\text{v}} \ , \tag{26}$$

where Q_{v} is the heat of vaporization and the subscripts l and v denote liquid and vapor respectively. To complete the system, a temperature boundary condition is needed at the interface. On a static phase boundary, the Clausius-Clapeyron relation holds, *i.e.* the phase boundary temperature is equal to the equilibrium saturation temperature and the pressure is continuous. At a dynamic phase boundary, by

Eq. (24), there is a pressure jump across the interface, and the equilibrium saturation temperatures of liquid and vapor are not equal, *i.e.*

$$T_{\mathrm{sat}}(p_{\mathrm{l}}) \neq T_{\mathrm{sat}}(p_{\mathrm{v}}) \ . \tag{27}$$

To determine the interface temperature, it is postulated that the temperatures of liquid and vapor at the interface are continuous. This approach was also used in [41]. Because the heat capacity of the liquid is large compared to that of the vapor, it is assumed that the equilibrium temperature on the dynamic phase boundary is $\overline{T} = T_{\mathrm{l}}$, where T_{l} is the liquid temperature given by the standard Riemann problem solution [42].

For the mass flux $M = \rho_{\mathrm{v}}(u_{\mathrm{v}} - s) = \rho_{\mathrm{l}}(u_{\mathrm{l}} - s)$, the mass and momentum balance equations give

$$M = -\frac{p_{\mathrm{v}} - p_{\mathrm{l}}}{u_{\mathrm{v}} - u_{\mathrm{l}}} \tag{28}$$

$$M^2 = -\frac{p_{\mathrm{v}} - p_{\mathrm{l}}}{\tau_{\mathrm{v}} - \tau_{\mathrm{l}}} \ , \quad \tau = \frac{1}{\rho} \tag{29}$$

$$(u_{\mathrm{v}} - s)(u_{\mathrm{l}} - s) = \frac{p_u - p_{\mathrm{l}}}{\rho_{\mathrm{v}} - \rho_{\mathrm{l}}} \ . \tag{30}$$

Combination of these equations with the energy balance equation leads to the generalized Hugoniot relation

$$\epsilon_{\mathrm{l}} - \epsilon_{\mathrm{v}} + \frac{p_{\mathrm{l}} + p_{\mathrm{v}}}{2}(\tau_{\mathrm{l}} - \tau_{\mathrm{v}}) = \frac{1}{M}(\kappa_{\mathrm{v}} T_{\mathrm{v},x} - \kappa_{\mathrm{l}} T_{\mathrm{l},x}) \ . \tag{31}$$

Heat transfer across the shock and rarefaction waves is neglected while it is accounted on the phase boundary.

The numerical algorithm for a dynamical phase transition proceeds as follows. Assuming the initial values of pressure, density, energy and also the temperature gradients on both sides of the interface are given, a standard Riemann problem for the compressible Euler equations without heat conduction is solved to obtain the

speed s for the motion of the the interface. Assuming that the vapor states are on the saturated liquid/vapor curve, the vapor pressure $p_{\rm v}$ is $p_{\rm v} = p(\overline{T})$. From the vapor EOS, the vapor density $\rho_{\rm v}$ is determined. Equations (31) and (29) are solved to get the mass flux M and liquid pressure $p_{\rm l}$. Then, the liquid-vapor velocity are computed from the mass balance equation (23).

$$u_{\rm l} = s + \frac{M}{\rho_{\rm l}} \tag{32}$$

$$u_{\rm v} = s + \frac{M}{\rho_{\rm v}} \ . \tag{33}$$

The solution above is called the phase boundary solution.

This is a new description of the Riemann problem associated with a phase transition in a fully compressible fluid. Unlike the solution of the standard Riemann problem in gas dynamics, which consists of piecewise constant states, and these states can be connected by shocks, rarefaction waves and contact discontinuities, the phase boundary solution is decoupled from acoustic waves, *i.e.* the states on the two sides of the phase boundary from the solution can not be connected to the initial values by these waves. It also should be noted that the assumption of the interface temperature made above is an approximation that needs further assessment.

6 Simulation Results

The algorithms described previously were used to simulate cavitation, jet breakup and spray formation. Fig. 6 shows a snap shot of the spray development. In the simulations, vapor bubbles were created inside the nozzle, then these bubbles were carried downstream outside the nozzle by the flow; while vapor bubbles were also formed after the jet left the nozzle. These vapor bubbles grew and broke the jet surface, forming spray and droplets.

The simulation predictions were compared with experimental data [9, 10, 11, 12]. These experimental data present mass *vs.* time in a 0.55 mm wide observation window which is centered 1 mm from the nozzle exit. The simulations predicted a peak mass, which is 20% to 35% higher than the experimental value. After the peak, the predicted mass is in a better agreement with the experimental values (see Fig. 7). The opening angle of the jet, (see Fig. 6), which varies as a function of time, is about 15 to 30 degrees and is in agreement with its experimental value. Fig. 8 shows a comparison of jet tip velocity computed from simulations with experimental data. Although the value computed from simulation predictions exhibits a wide variability, on the average, it is in agreement with the value computed from the experiment. It should be noted that the experimental data has been averaged over 100 injection cycles to remove fluctuations.

7 Conclusions

Direct numerical simulations of jet breakup using the front tracking approach were performed. Two EOS models were employed, *i.e.* a homogenized model and a discrete vapor bubble model with vapor bubbles of finite size. In the homogenized model, the properties of the vapor-liquid mixture are obtained by averaging the properties of the two fluids. In the discrete vapor bubble model, the vapor-liquid mixture is modeled as pure phase domains by vapor bubbles of finite size inserted into the diesel liquid and separated with liquid by interfaces. A dynamic bubble creation algorithm was formulated to allow vapor bubble insertion, and a new description of the Riemann problem associated with a phase transition was developed. The critical vapor bubble size and the bubble population are described by using the homogeneous nucleation model.

Although the homogenized EOS model predicted inception of cavitation, there was a slow growth of surface perturbations that failed to produce jet breakup.This is attributed to the suppression of KH instabilities in a high Mach number flow. The discrete vapor bubble model predicted cavitating regions made of many microbubbles that led to jet breakup. The results indicate that the direct numerical simulation of breakup and atomization in a high speed jet is critically dependent on the use of an EOS model which, in combination with front-tracking, allows the representation of the two phase mixture as two distinct fluids separated by a sharp interface. Finally, this work was mainly focused on the simulation of the two-phase mixture resulting from cavitation, and the influence of other parameters on spray formation is a subject of further research.

References

[1] R. D. Reitz and F. V. Bracco. Mechanism of atomization of a liquid jet. *Phys. Fluids*, 25:1730–1742, 1982.

[2] O'Rouke and A.A. Amsden. The tab method for numerical calculation of spray droplet breakup. *SAE Paper*, 872089, 1987.

[3] Tanner. Liquid jet atomization and droplet breakup modeling of non-evaporating diesel fuel spray. *SAE Paper*, 970050, 1997.

[4] E.A. Ibrahim, H.Q. Yang, and A.J. Przekwas. Modeling of spray droplet deformation and breakup. *AIAA J. Propulsion and Power*, 9:651–654, 1993.

[5] B. Bukiet, C. L. Gardner, J. Glimm, J. W. Grove, J. Jones, O. McBryan, R. Menikoff, and D. H. Sharp. Applications of front tracking to combustion, surface instabilities and two-dimensional Riemann problems. In *Transactions*

of the Third Army Conference on Applied Mathematics and Computing, ARO Report No. 86–1, pages 223–243, 1986.

[6] J. Glimm, M. J. Graham, J. W. Grove, X.-L. Li, T. M. Smith, D. Tan, F. Tangerman, and Q. Zhang. Front tracking in two and three dimensions. *Comput. Math. Appl.*, 35(7):1–11, 1998.

[7] J. Glimm, J. W. Grove, X.-L. Li, K.-M. Shyue, Q. Zhang, and Y. Zeng. Three dimensional front tracking. *SIAM J. Sci. Comp.*, 19:703–727, 1998.

[8] J. Glimm, J. W. Grove, X.-L. Li, and D. C. Tan. Robust computational algorithms for dynamic interface tracking in three dimensions. *SIAM J. Sci. Comp.*, 21:2240–2256, 2000.

[9] Andrew MacPhee, Mark Tate, and Christopher Powell *et al.* X-ray imaging of shock waves generated by high pressure fuel sprays. *Science*, 295:1261–1263, 2002.

[10] C. F. Powel, Y. Yue, Sreenath Gupta, Armon McPherson, R. Poola, and J. Wang. Development of a quantitative measurement of a diesel spray core using synchrotron X-rays. In *Eighth International Conference on Liquid Atomization and Spray Systems, Pasadena, CA*, 2000.

[11] C.F. Powel, Y. Yue, R. Poola, and J. Wang. Time resolved measurements of supersonic fuel sprays using synchrotron x-rays. *J. Synchrotron Rad.*, 7:356–360, 2000.

[12] C. F. Powel, Y. Yue, R. Poola, J. Wang, M. Lai, and J. Schaller. Quantitative X-ray measurements of a diesel spray core. In *Proc. 14th Annual Conference on Liquid Atomization and Spray Systems (ILASS)*, Dearborn, MI, 2001.

[13] R. D. Reitz and F. V. Bracco. *Mechanisms of breakup of round liquid jets.* The Encyclopedia of Fluid Mechanics. Gulf Pub. Co., Book Division, 1986.

[14] S. P. Lin and R. D. Reitz. Drop and spray formation from a liquid jet. *Annu. Rev. Fluid Mech.*, 30:85–105, 1998.

[15] S. Chandrasekhar. *Hydrodynamic and Hydromagnetic Stability.* Dover Publications, New York, 1981.

[16] W. Bergwerk. *Proceedings of the Institution of Mechanical Engineers*, 173(25):655–660, 1959.

[17] H. Chaves and *et al.* Experimental study of cavitation in the nozzle hole of diesel injectors using transparent nozzles. *SAE Paper*, No. 950290:199–211, 1995.

[18] C. Arcoumanis, M. Gavaises, J.M. Nouri, E. Abdul-Wahab, and Roy. W. Horrocks. Analysis of the flow in the nozzle of a vertical multi hole diesel engine injector. *SAE Paper 980811*, 1998.

[19] D. P. Schmidt, C. J. Rutland, and M. L. Corradini. Cavitation in two-dimensional asymmetric nozzles. SAE 1999-01-0518, February 1999. SAE International Congress.

[20] C. Heimgartner and A. Leipertz. Investigation of the primary spray breakup close to the nozzle of a common-rail high pressure diesel injection system. In *Proc. ICLASS 2000*, pages 1235–1241, 2000.

[21] M. Berger and P. Colella. Local adaptive mesh refinement for shock hydrodynamics. *J. Comp. Phys.*, 82:64–84, 1989.

[22] P. Colella. A direct Eulerian MUSCL scheme for gas dynamics. *SIAM Journal on Computing*, 6(1):104–117, 1985.

[23] J. Glimm, X.-L. Li, and Z.-L. Xu. Front tracking algorithm using adaptively refined meshes. In *Proceedings of the 2003 Chicago Workshop on adaptive Mesh Refinement Methods*. 2004. the Lecture Notes in Computational Science and Engineering, ISSN: 1439-7358.

[24] H. Schlichting. *Boundary layer Theory*. Mcgraw-Hill Book Company Inc., New York, 1960.

[25] H. Kirsten. *Experimentelle Untersuchungen der Entwicklung der Geschwindigkeitsverteilung der turbulenten Rohrstromung*. PhD thesis, Leipzig, 1927.

[26] W. Szablewski. Der einlauf einer tubulenten rohrstromung. *Ing. Arch*, 21:323–330, 1953.

[27] G. Wallis. *One-Dimensional Two-Phase Flow*. McGraw-Hill, New York, 1969.

[28] R. Samulyak and Y. Prykarpatskyy. Richtmyer-meshkov instability in liquid metal flows: influence of cavitation and magnetic fields. *Mathematics and Computers in Simulations*, 65:431–446, 2004.

[29] J. Glimm, X. L. Li, W. Oh, A. Marchese, M.-N. Kim, R. Samulyak, and C. Tzanos. Jet breakup and spray formation in a diesel engine. In *Proceedings of the Second MIT Conference on Computational Fluid and Solid Mechanics*. Cambridge, MA, 2003. SUNY Stony Brook preprint No. susb-ams-02-20.

[30] John W. Miles. On the disturbed motion of a plane vortex sheet. *J. Fluid Mech.*, 4:538–552, 1958.

[31] T. Foglizzo and M. Ruffert. An analytic study of bondi-hoyle-lyttleton accretion. *Astronomy and Astrophysics*, 347:901–914, 1999.

[32] C. E. Brennen. *Cavitation and Bubble Dynamics*. Oxford University Press, New York, 1995.

[33] L. Landau and E. Lifshitz. *Statistical Physics*. Pregamon Press Ltd, Oxford, UK, 1980.

[34] S. Balibar and F. Caupin. Metastable liquids. *J. of Physics: Condensed Matter*, 15:s75–s82, 2003.

[35] T. Lu, R. Samulyyak, and J. Glimm. Direct numerical simulation of bubbly flows and its application. *Submitted to J. of Physics of Fluids*, 2004.

[36] R. Samulyak, T. Lu, Y. Prykarpatskyy, J. Glimm, Z. Xu, and M.N. Kim. Comparison of direct and homogeneous numerical approaches to cavitation modeling. *submitted to Int. J. For Multiscale Comp. Eng.*, 2004.

[37] Damir Juric and G. Tryggvason. Computations of boiling flows. *Int. J. Multiphase Flow*, 24(3), 1998.

[38] Lord Rayleigh. On the pressure developed in a liquid during the collapse of a spherical cavity. *Phil. Mag*, 34:94–98, 1917.

[39] M.S. Plesset and A. Prosperetti. Vapor bubble growth in a superheated liquid. *J. Appl. Phys.*, 85:349–368, 1978.

[40] W. J. Welch. Local simulation of two-phase flows including interface tracking with mass transfer. *J. Comp. Phys.*, 12:142–154, 1995.

[41] A. Huang and D. D. Joseph. Instability of the equilibrium of a liquid below its vapor between horizontal heated plates. *J. Fluid Mech.*, 242:235–247, 1992.

[42] J. Smoller. *Shock Waves and Reaction-Diffusion Equations.* Springer-Verlag, New York, 1983.

List of Figure Captions

Figure 1: Geometry of injection reservoir and nozzle leading to combustion chamber.

Figure 2: Vorticity in the nozzle.

Figure 3: The pressure field of the flow at consequent times. (The unit of pressure is bar. Pressure above 0 bars is represented as white color.)

Figure 4: The P vs. V isentrope for diesel fuel.

Figure 5: The density plot of the diesel jet from the homogenized EOS model simulation.

Figure 6: Plot of jet interface at late time.

Figure 7: Plot of mass through a narrow window located 1 mm from the nozzle exit.

Figure 8: Plot of jet tip velocity.

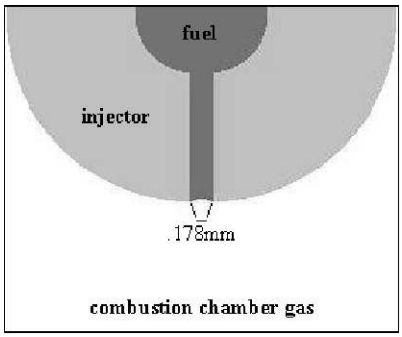

Figure 1: Geometry of injection reservoir and nozzle leading to combustion chamber.

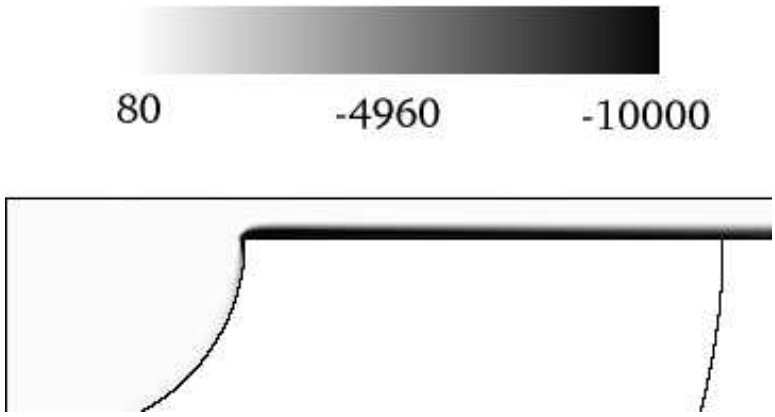

Figure 2: Vorticity in the nozzle

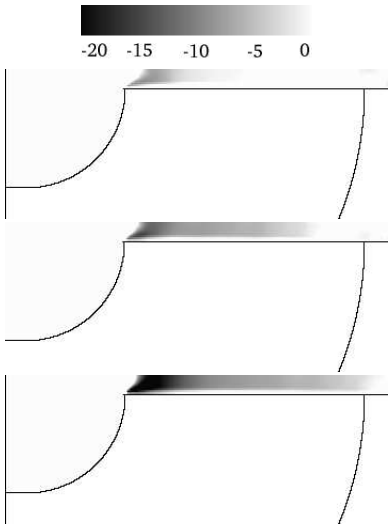

Figure 3: The pressure field of the flow at consequent times. (The unit of pressure is bar. Pressure above 0 bars is represented as white color.)

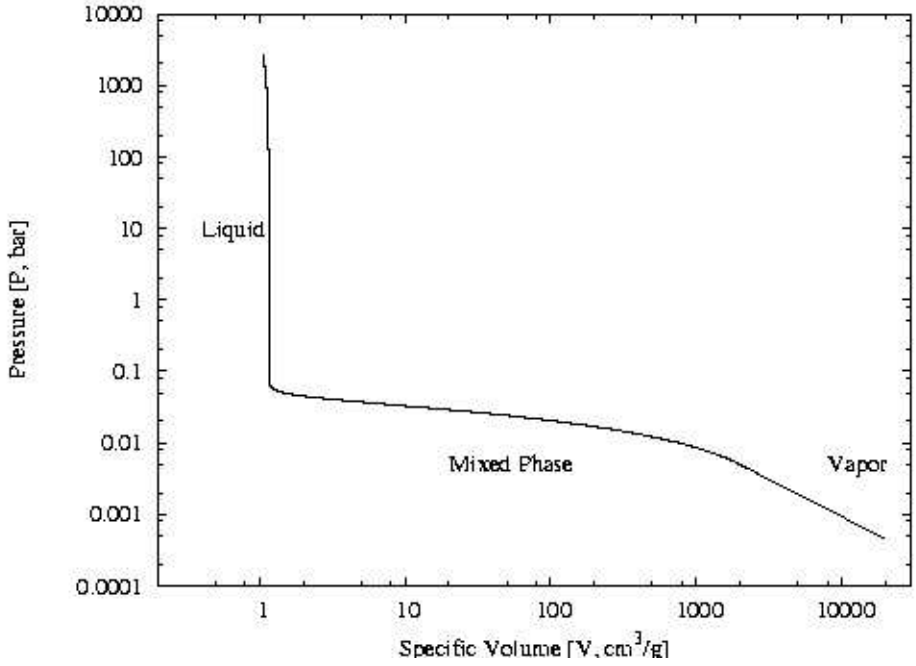

Figure 4: The P vs. V isentrope for diesel fuel.

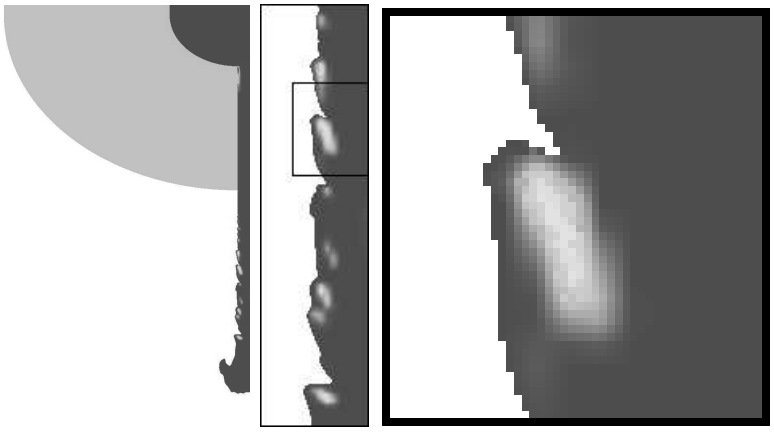

Figure 5: The density plot of the diesel jet from the homogenized EOS model simulation.

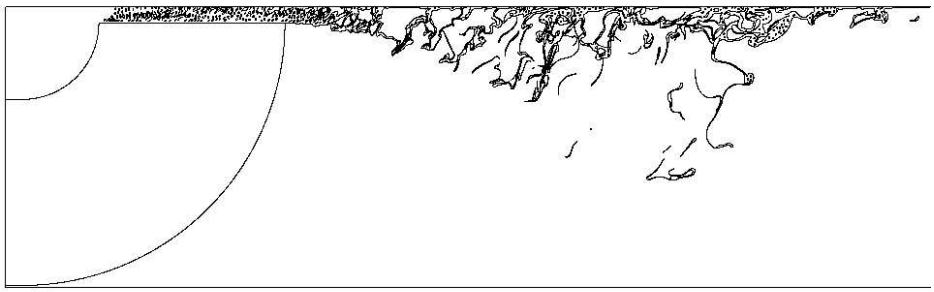

Figure 6: Plot of jet interface at late time.

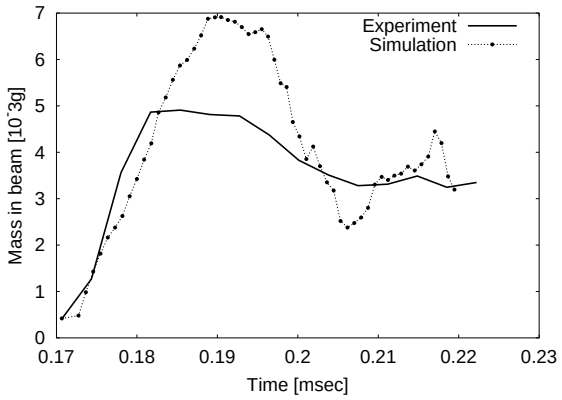

Figure 7: Plot of mass through a narrow window located 1 mm from the nozzle exit.

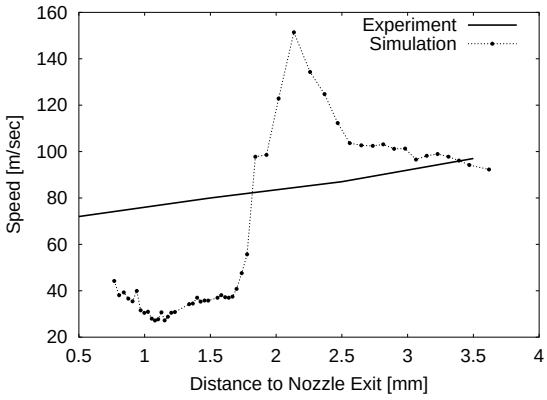

Figure 8: Plot of jet tip velocity.